The Planetary Science Journal, 4:89 (22pp), 2023 May https://doi.org/10.3847/PSJ/acbeab

Lunar Laser Ranging Retroreflectors: Velocity Aberration and Diffraction Pattern

James G. Williams[1], Luca Porcelli[2], Simone Dell'Agnello[2], Lorenza Mauro[2], Marco Muccino[2,3], Douglas G. Currie[4], Dennis Wellnitz[4], Chensheng Wu[4,5], Dale H. Boggs[1], and Nathan H. Johnson[2]
[1] Jet Propulsion Laboratory, California Institute of Technology, Pasadena, CA 91109-8099, USA; James.G.Williams@jpl.nasa.gov
[2] National Institute for Nuclear Physics—Frascati National Labs (INFN—LNF), Frascati (Rome), Italy
[3] aeroTecno s.r.l., Rome, Italy
[4] University of Maryland, College Park, MD 20742, USA
[5] KBR, Inc., Greenbelt, MD 20770, USA
Received 2022 June 27; revised 2023 February 20; accepted 2023 February 22; published 2023 May 18

Abstract

The Lunar Laser Ranging (LLR) retroreflector arrays have been on the Moon for half a century. During that time, the laser range uncertainty has improved by a factor of 100. Consequently, the science results have also improved by orders of magnitude. New retroreflectors are scheduled to go to the Moon on Commercial Lander Payload Services missions and the Lunar Geophysical Network mission. The new retroreflectors are single 10 cm corner cube retroreflectors that will not spread the laser pulse during reflection like the existing arrays do. Due to the orbital and Earth rotational speeds, there is a velocity aberration of 0.″8–1.″5 for existing stations. Larger corner cubes require attention to ensure that the spread of possible velocity aberration displacements is optimally contained within the diffraction pattern. The diffraction pattern can be changed by making one or more of the rear dihedral angles slightly different from 90°. Improvements in the equipment at the LLR stations and improvements in the data analysis software are also desirable. Future possibilities are described.

Unified Astronomy Thesaurus concepts: Space vehicle instruments (1548); The Moon (1692); Earth-moon system (436)

1. Introduction

For half a century Lunar Laser Ranging (LLR) has provided science results for lunar geophysics and geodesy, gravitational physics, and terrestrial geodesy. It has also provided a lunar orbit and lunar orientation with small uncertainty that is used by missions to the Moon. A recent review of LLR is given by Müller et al. (2019). A discussion of solar system tides is given by Bagheri et al. (2022). The case for new geophysical instruments on the Moon, including new laser retroreflectors, is made by Haviland et al. (2022) and Kawamura et al. (2022).

Four observatories on Earth fire short laser pulses toward each one of five retroreflector sites on the Moon, a pulse bounces off of the site's corner cubes, and then it returns to the observatory on Earth. The round-trip time of flight gives a distance since the speed of light has a defined value (Mohr et al. 2016). The mean geocentric distance of the Moon is 385,000.5 km (Chapront-Touzé & Chapront 1988). Current data analyses fit modern ranges with a 9 mm weighted rms residual, 2.3×10^{-11} relative to the distance.

The five existing lunar retroreflectors are arrays of corner cube prisms. Each prism returns an incoming beam of light back toward its source. The Apollo 11 and 14 reflectors have 100 corner cube or cube corner retroreflectors (CCRs) that are 3.8 cm in diameter; see Figure 1. Apollo 15 has 300 prisms. Lunokhods 1 and 2 have 14 larger triangular CCRs, but the exiting light is hexagonal. The three rear faces of a solid CCR may be uncoated using total internal reflection (TIR), or they may be coated with a reflecting material. The 10 cm Next Generation Laser Retroreflector (NGLR) and MoonLIGHT CCRs of this paper are solid fused silica with an index of refraction of 1.46 that use TIR. Hollow CCRs can be made by bonding three flat reflecting surfaces at their common edges (Merkowitz et al. 2007; Preston & Merkowitz 2013, 2014; Turyshev et al. 2013), but they are difficult to construct. Studies of all three types were made by Otsubo et al. (2010), and a study of hollow reflectors was made by Otsubo et al. (2011). Information on existing and future CCRs is given in Table 1.

Since the arrays of CCRs rarely have the normal to the array front face exactly in the direction of the laser beam, the deviation is typically 0.1 rad, there is spreading of the photons in the return pulse. The spreading is about 0.1 rad × array dimension/2. The Appendix of Williams et al. (2022) has detailed calculations that give maximum pulse spreads of ±3 cm for the Lunokhods, ±6 cm for Apollos 11 and 14, and ±11 cm for Apollo 15. Consequently, normal points with small uncertainties, constructed by combining ranges from multiple firings, require many returned photons. A next step for LLR is to place large single CCRs on the Moon that will not spread the pulse on reflection. Since the strength of the reflected pulse depends on the fourth power of the CCR's diameter (two powers for area and two powers for the diffraction pattern size), a single CCR with a diameter of 10 cm should be about half as effective as the original Apollo 11 and 14 arrays. However, the Apollo and Lunokhod arrays are thought to have a thin layer of dust that degrades their performance (Murphy et al. 2010, 2014). Consequently, the 10 cm CCRs are expected to be brighter than the existing small reflectors. A 10 cm CCR requires careful design, construction, and testing.

This paper describes the new 10 cm CCRs and their design considerations. These larger CCRs will allow improved range uncertainty. The larger CCRs have a narrower diffraction pattern than the Apollo CCRs. Consequently, the spread of velocity aberrations (VAs) should be placed near the peak of

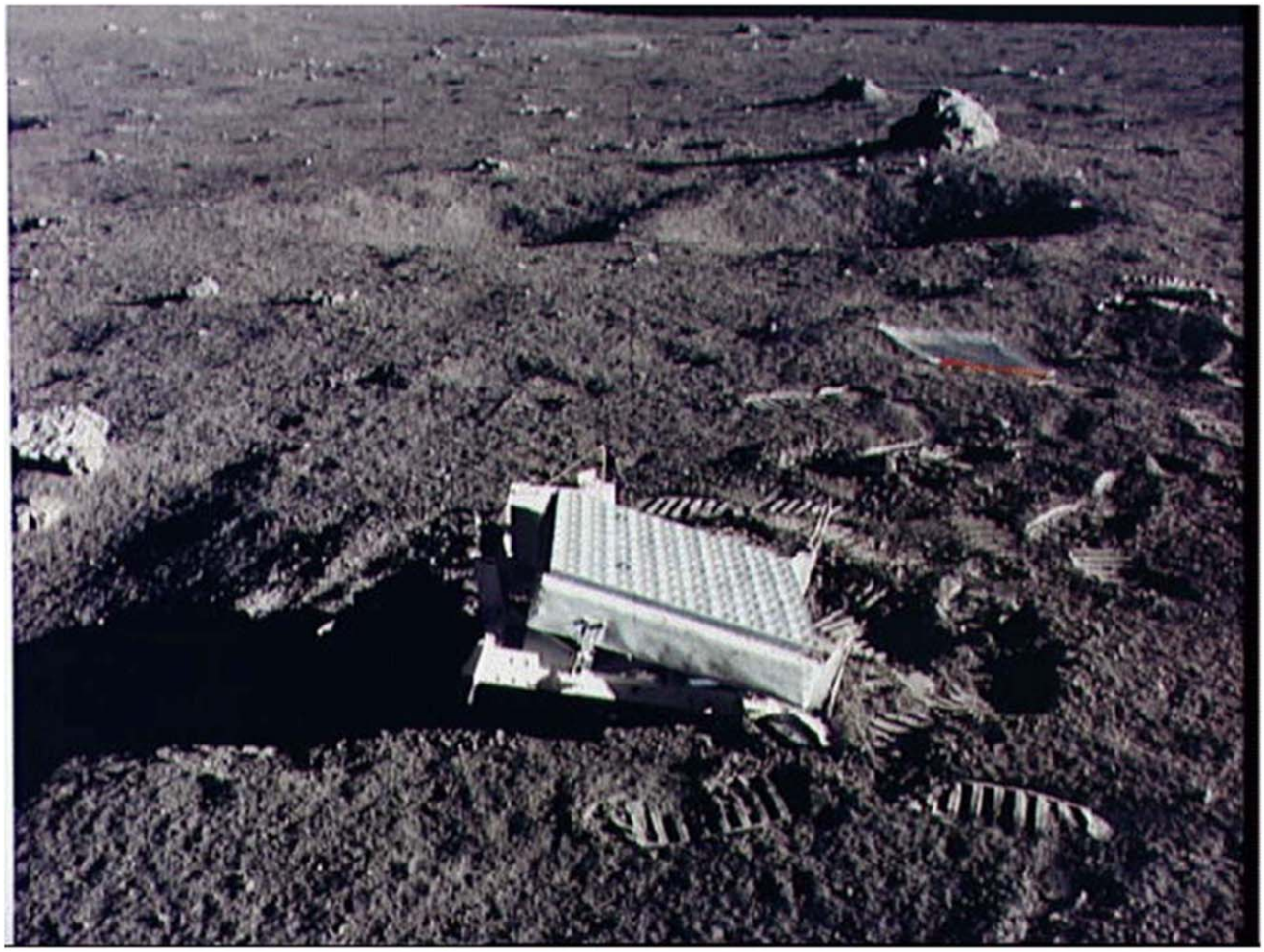

Figure 1. The Apollo 14 retroreflector has a 10 × 10 array of corner cube prisms. Picture from NASA.

Table 1
Information on Existing and Future Lunar Retroreflectors

Site	Number of CCRs	Array Size (cm × cm)	CCR Aperture	CCR Size (cm)	Area (cm^2)	Reflection
Apollo 11 and 14	100	46 × 46	circle	3.8	1134	TIR
Apollo 15	300	105 × 65	circle	3.8	3400	TIR
Lunokhod 1 and 2	14	44 × 19	hexagon	7.1 × 6.2	458	Silver
NGLR	1	10	circle	10.0	79	TIR
MoonLIGHT	1	10	circle	10.0	79	TIR

the far-field diffraction pattern (FFDP). Along with the new CCRs, improvements in the ranging stations' equipment and in the data analysis model would take advantage of the expected better range uncertainty.

2. History of Range Uncertainty

Prior to the first Apollo landing, the lunar orbit and orientation were determined from optical measurements of angles. At the 385,000.5 km mean distance of the Moon (Chapront-Touzé & Chapront 1988), an angle of 1″ is equivalent to 1.87 km. So subarcsecond measurement uncertainties were equivalent to position uncertainties of hundreds of meters.

At a first approximation, the Moon rotates synchronously every 27.322 days and its equator precesses along the ecliptic plane uniformly with time (18.6 yr retrograde period). More exactly, the rotation angle speeds up and slows down by about ±150″, and the pole that is normal to the equator plane varies about ±150″ × 100″ in two orthogonal directions. These oscillations about uniform rotation and precession are called physical librations. These variations can be represented with Fourier series. The size and phase of various periodic physical libration terms carry lunar science information. Since the lunar orbit is ∼221 times larger than the Moon, the physical librations are only ±0.″7 as seen from Earth. Except for the 1.°54 mean tilt of the lunar equator to the ecliptic plane, the orientation of the Moon was very difficult to measure from optical angles.

The first retroreflector was placed on the Moon in 1969 by the Apollo 11 astronauts. Early ranges had meter-level uncertainties, but this was improved to a few decimeters by early 1970. Within a few months the measurement uncertainty went from hundreds of meters, to meters, to decimeters. Subsequent improvements brought the range uncertainty down

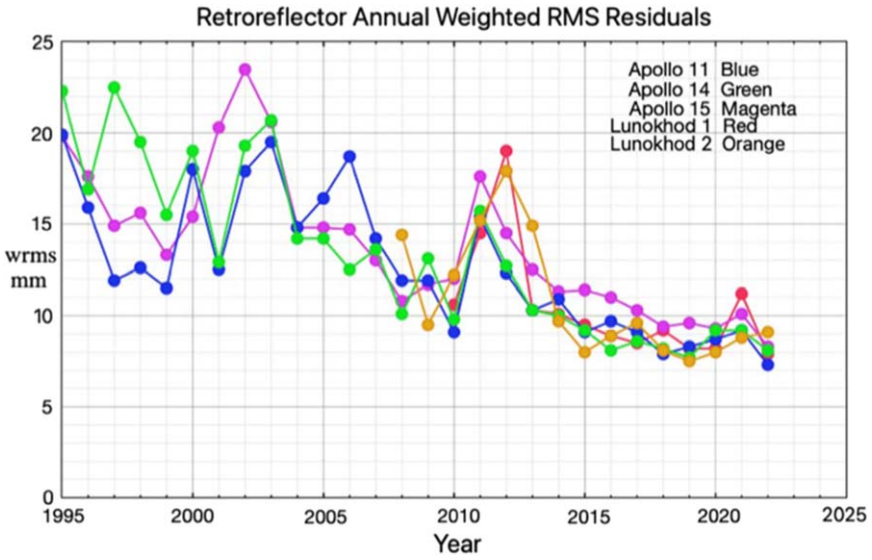

Figure 2. The annual weighted rms residuals for each CCR for 1995 to 2022.

to 2 cm in 1995 and <1 cm today. With the existing arrays, the pulse is spread at the bounce by several centimeters owing to the varying array orientations. Single 10 cm CCRs would eliminate that spread during the bounce of the pulse. The smaller received pulse width motivates improvements in equipment at the ranging stations.

There is an additional reason to deploy new retroreflectors on the Moon. Dust on the faces of the existing CCRs appears to have degraded signal strength (Murphy et al. 2010, 2014). Sunlight shining on any dust on the front face of a CCR causes a thermal gradient that causes a refractive index gradient that spreads the angular width of the return beam (Goodrow & Murphy 2012).

Each range has an associated uncertainty. The weight for each range is $1/\text{uncertainty}^2$. The weighted rms (wrms) residuals for each year from 1995 to 2022 are shown in Figure 2 for each of the five existing CCRs. Prior to 2008, most years for Lunokhod 2 had only one or two ranges, so we have deleted those noisy points. Lunokhod 1 was found in 2010 after being lost for decades (Murphy et al. 2011). The OCA/MeO station started IR ranging in 2015, benefiting the detection of the two Lunokhods. The wrms residuals improved in about 2008. Note that the Apollo 15 wrms residual is above the four smaller reflectors. Although the roughly 1.5 mm difference of recent years may seem small, independent errors add in a sum square manner. Consequently, Apollo 15 has about 5 mm more noise than the smaller reflectors. Presumably, this difference is due to the larger size of the Apollo 15 CCR. We note that signal strength and range uncertainty are affected by several factors.

3. New CCRs

The larger a CCR, the more difficult it is to prevent thermal and index of refraction gradients when illuminated by sunlight. A 10 cm diameter has been chosen for the new CCRs. The first new 10 cm CCRs have been fabricated, and two have been placed in mountings.

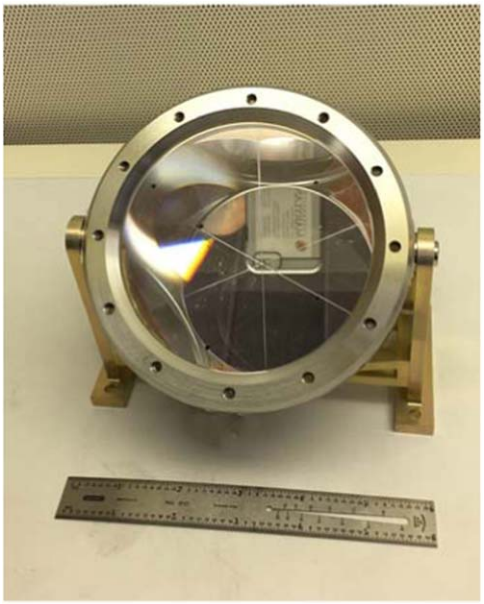

Figure 3. A 10 cm NGLR CCR at the University of Maryland, with contributions to the midlatitude support structure from INFN.

3.1. NGLR

The NGLR retroreflector consists of a single large CCR (Currie et al. 2013); see Figure 3. The core-NGLR consists of a single 10.0 cm fused silica CCR. Total internal reflection is used.

The CCR is surrounded by a housing to protect the CCR from thermal radiation from the regolith. Thermal radiation would cause thermal gradients in the CCR, causing gradients in the index of refraction, which would spread the return laser pulse pattern over a wider region on Earth (Goodrow & Murphy 2012). A mechanism to support the CCR is provided by the Support-NGLR, which is the interface between the core-NGLR and the lander (Currie et al. 2013), or the regolith, or the anchored support (Zacny et al. 2012). The support depends in detail on the method of transport to the Moon and the method of deployment.

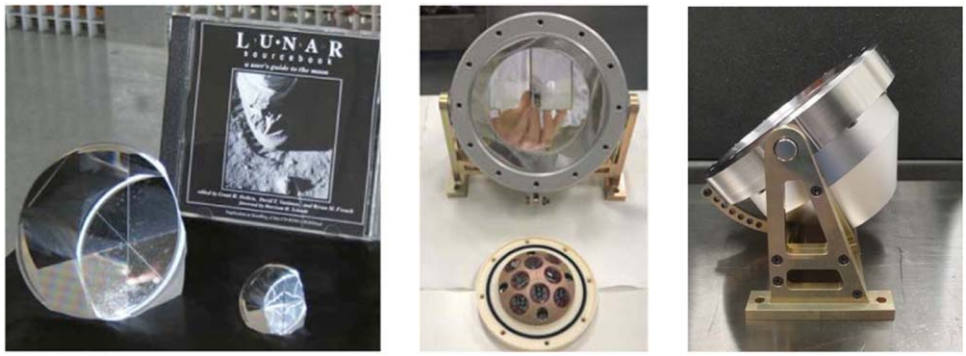

Figure 4. Left: a new 10 cm CCR next to an Apollo 3.8 cm CCR; middle: a 10 cm CCR in a mount next to a Martian retroreflector for orbital downward ranging; right: a MoonLIGHT corner cube in a mount.

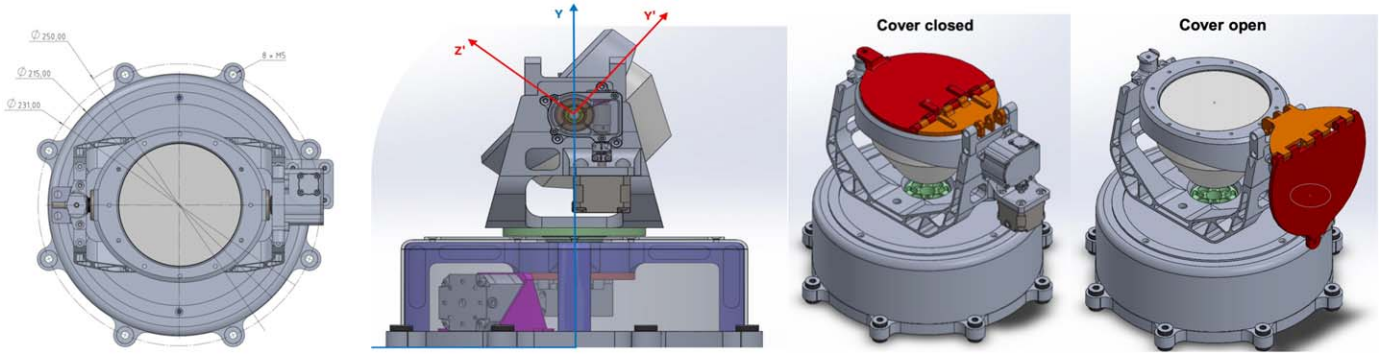

Figure 5. The two views on the left show a next-generation CCR in an MPAc mount; the two views on the right show the dust cover closed and open (credit ESA).

Table 2
Information on the Two New CCRs Scheduled for Future Lunar Landings

Site	CCR	Type	Diam (cm)	Long	Lat	Landing	ME Az	ME El
Mare Crisium	NGLR	Solid	10	61.°81E	18.°56N	Middle 2024	260.°32	26.°37
Reiner Gamma	MoonLIGHT	Solid	10	59.°0W	7.°5N	Spring 2024	94.°48	30.°48

The laser light exiting from the CCR has six segments, each with its own polarization. Nonzero dihedral angle offsets (DAOs) overlap the segments with different polarizations, complicating the calculation of the off-axis return signal strength in the FFDP. Consequently, the position of the peak signal may shift in a nonlinear manner with increasing DAO.

3.2. MoonLIGHT

The MoonLIGHT retroreflector is also a 10 cm solid fused silica CCR that uses total internal reflection. The NGLR and MoonLIGHT retroreflectors are scaled-up versions of the Apollo 3.8 cm CCRs; see the left panel of Figure 4. The foregoing concerns apply for thermal effects on optical quality and thermal expansion and contraction of the support structure.

The Apollo lunar retroreflector arrays were aligned by astronauts to point at the center of Earth with compensation for lunar optical librations at the time they were put in place. With the MoonLIGHT Pointing Actuator (MPAc), this alignment with the mean Earth (ME) direction will be performed robotically by two actuators; see Figure 5. There is dust protection during landing and active ME pointing after landing. The deployment of next-generation retroreflectors for fundamental physics and lunar and terrestrial geophysics is a goal of ESA's and NASA's Strategy for Science at the Moon (Crawford et al. 2012; ESA 2019; NASA 2019; Porcelli et al. 2021; Turyshev et al. 2021).

With new CCRs on the Moon, we look forward to further improvements in range uncertainty and the resulting science.

4. Schedule

The first NGLR CCR is scheduled to go to Mare Crisium on the Moon in mid-2024 on a Firefly lander, and the first MoonLIGHT CCR is scheduled to go to Reiner Gamma in spring of 2024 on an Intuitive Machines lander. The nominal landing sites are at 61.°81E by 18.°56N for the Mare Crisium site and 59.°0W by 7.°5N for the Reiner Gamma site. Reiner Gamma is a bright "swirl" located at a magnetic anomaly. These two CCRs will be carried by landers under the Commercial Lander Payload Services (CLPS) missions. Table 2 gives some information about these two sites. The azimuth and elevation angles of the ME directions are given.

5. Velocity Aberration

Since the laser source is moving with respect to the CCR, as seen from the Moon the apparent positions of the Earth station at the transmit and receive times will be different. This aberration due to velocity v is $2v/c$ in radians or $412{,}530v/c$ in seconds of arc, where c is the speed of light. Velocity v is the

Table 3
Distribution, Normalized to a Peak Value of 1000, of Velocity Aberration in Lunar Longitude and Latitude for Ranges to Mare Crisium from OCA/MeO for Elevations ⩾20°

Lat (arcsec)	Lat (arcsec)	1.″5–1.″4	1.″4–1.″3	1.″3–1.″2	1.″2–1.″1	1.″1–1.″0	1.″0–0.″9	0.″9–0.″8
0.3	0.4	6	38	72	108	201	144	2
0.2	0.3	8	54	144	269	531	455	44
0.1	0.2	7	47	150	313	618	540	76
0.0	0.1	8	84	261	522	998	836	100
−0.1	0.0	7	82	260	522	1000	835	100
−0.2	−0.1	6	45	149	313	618	541	77
−0.3	−0.2	8	52	144	269	534	456	44
−0.4	−0.3	5	37	72	109	201	145	2

Table 4
Extremes of Longitude and Latitude Aberration for Ranges from Four Stations

Site	Stn	Lat Min (arcsec)	Lat Max (arcsec)	Lng Min (arcsec)	Lng Max Elev > 20° (arcsec)	Lng Max Elev > 10° (arcsec)	Lng Max Elev > 0° (arcsec)
Mare Crisium	APO	–0.39	0.39	0.79	1.44	1.57	1.69
Reiner Gamma	APO	–0.39	0.39	0.79	1.44	1.57	1.69
Mare Crisium	MAT	–0.37	0.37	0.84	1.48	1.60	1.71
Reiner Gamma	MAT	–0.37	0.37	0.84	1.48	1.60	1.71
Mare Crisium	OCA	–0.36	0.36	0.87	1.49	1.60	1.72
Reiner Gamma	OCA	–0.35	0.35	0.87	1.49	1.60	1.72
Mare Crisium	WZL	–0.34	0.34	0.91	1.51	1.63	1.74
Reiner Gamma	WZL	–0.34	0.34	0.91	1.51	1.63	1.75

component perpendicular to the line of sight. The orbital speed of the Moon is about 1.0 km s^{-1}, and the equatorial rotational velocity of Earth is 465 m s^{-1}. The equator plane of Earth is tilted by 23.°44 to the ecliptic plane, whereas the lunar equator is tilted by 1.°54 to the ecliptic plane. The French LLR station at 43.°6 north rotates at 337 m s^{-1}. There is variety in the orientations of Earth and the Moon with respect to one another and with respect to the ecliptic plane. In addition, the lunar orbit is not circular, so its orbital speed varies ±0.1 km s^{-1}. Considering these complexities, the size of the aberration varies, and we present a distribution function for the VA in lunar longitude and latitude as seen from the CCR site (Table 3).

5.1. Aberration Distribution

The first NGLR retroreflector is scheduled to go to Mare Crisium in mid-2024, and the first MoonLIGHT CCR is scheduled to go to Reiner Gamma in the spring of 2024. The distribution of aberration versus lunar longitude and latitude is given in Table 3 for the Mare Crisium site. The French station (OCA/MeO) at 43.°6N was used for the Earth station. A 20° elevation limit was used for the station. For example, the most probable aberration for Mare Crisium is between 1.″0 and 1.″1 in longitude and is slightly south of the lunar equator. The lack of north–south symmetry is because the ranging station is not at the center of Earth and the retroreflector is not at the center of the Moon. We make longitude aberration increase to the left since that is how it would appear in the lunar sky. The Reiner Gamma distribution is very similar, so we only present the Mare Crisium case.

The azimuths of the ME directions in Table 2 are not zero. Consequently, from the Mare Crisium site the Table 3 pattern would appear rotated clockwise by 80° = 180° − 100° with respect to horizontal, and from the Reiner Gamma site the pattern would appear rotated counterclockwise by 86° = 180° − 94°. The longitude aberration is nearly vertical for Mare Crisium and downward for Reiner Gamma.

The minimum and maximum latitude and longitude aberrations are given in Table 4 for four stations: the Apache Point Observatory in the USA (APO), the Matera station in Italy (MAT), the OCA/MeO station in France, and the Wettzell station in Germany (WZL). The longitude maximum depends on the elevation limit, but the longitude minimum and the latitude extrema have little sensitivity to elevation. Lower-latitude stations have larger spreads of aberration. APO has a latitude of 32.°6N, MAT is at 40.°5N, OCA/MeO is at 43.°6N, and WZL sits at 49.°0N.

In Figure 6 are shown lunar longitude and latitude extremes of aberration for station latitudes of 0°, 30°, and 60° for elevations >20°. The spot at 0″, 0″ is the apparent direction of the incoming laser beam. The strongest part of the CCR diffraction pattern needs to match the appropriate box for the station latitude. Terrestrial elevations below 20° extend the boxes farther east. The boxes are not quite rectangular, with rounded corners and curved latitude extrema. Ideally, we want the diffraction pattern to enclose a region bounded by 0.″8–1.″5 in lunar longitude and ±0.″4 in latitude for existing stations and 0.″7–1.″5 in lunar longitude and ±0.″43 in latitude to accommodate possible stations nearer the equator.

6. Far-field Diffraction Pattern

The advantages of 10 cm lunar CCRs were discussed by Martini et al. (2012), Garattini et al. (2013), Currie et al. (2013), and Ciocci et al. (2017). The first 10 cm CCRs are now being prepared for delivery to the Moon.

A perfect corner cube retroreflector reverses the direction of an incoming laser beam, but the reflected beam has a diffraction pattern. Code V is software developed by Synopsys to model, optimize, and investigate optical systems for several applications.

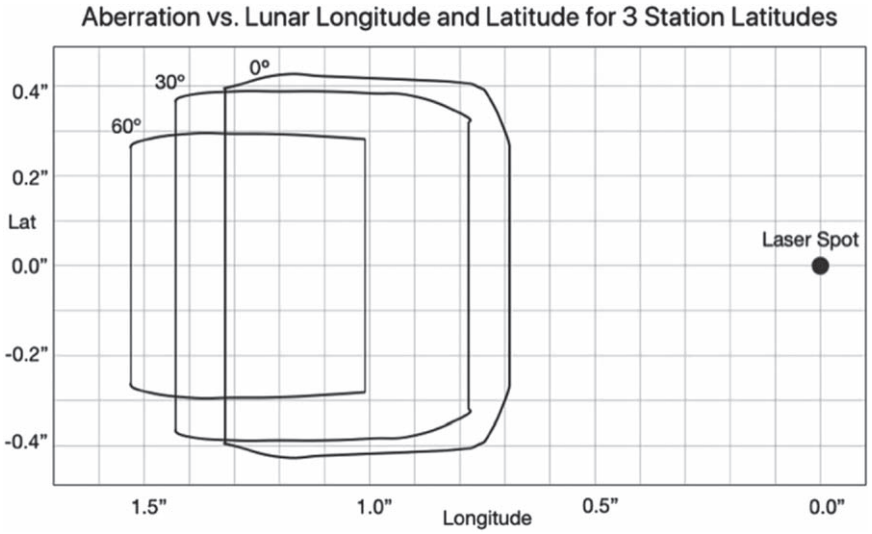

Figure 6. VA for three Earth station latitudes as seen from the lunar center of mass vs. lunar longitude and latitude.

At the Satellite/lunar/GNSS laser ranging Characterization Facilities Lab of INFN-LNF, Code V is utilized to simulate the optical performances of single (or arrays of) CCRs employed in space missions. These simulations are compared with the optical experimental data obtained from tests on the actual payloads (Ciocci et al. 2017).

Code V features a graphical user interface that enables command entry and simulation execution. The software is also user-friendly because it supports the use of macros written in Macro PLUS programming language. These macros can be written on a text editor and then interpreted by the software. To initialize the simulation of the specific CCR under examination, some key parameters are required:

1. the diameter (or aperture);
2. the DAOs;
3. the type of polarization;
4. the laser beam wavelength;
5. the incidence angle of the laser beam on the CCR front face;
6. the material;
7. the reflectivity.

Additionally, the grid's dimensions and spacing are appropriately entered to produce an image with the desired resolution and size. Each run produces three plots:

1. the average laser return's FFDP;
2. the laser return as a function of the VA averaged over the azimuth angle;
3. the laser return of the total pattern as a function of the azimuth angle for a fixed VA.

In all of these plots, the laser return strength is quantified in absolute Optical Cross Section (OCS) units.

6.1. MoonLIGHT/NGLR Simulations for Linear Polarization

For station latitudes of 30°–50°, the most probable VA is between 1.″0 and 1.″1 (or, equivalently, between 4.84 and 5.33 rad) in longitude and is slightly south of the lunar equator, as Table 3 shows.

Considering the wide range of VAs shown in Table 3, we wish to understand whether introducing nonzero DAOs for MoonLIGHT/NGLR CCRs would increase laser return strength or not. This is an optimization problem because

1. finite DAOs shift the laser return intensity from the central peak of the FFDP to the diffraction rings (and thus to higher values of VA), depending on the value of the DAOs;
2. the above shift causes an overall decrease of the intensity of the central peak of the FFDP in favor of the diffraction rings; and
3. both of the above two effects are not linear, and thus it is difficult to give a simple analytic guess.

In view of the above, Code V simulations are crucial to understand/solve this issue. We input the following key parameters:

1. diameter $D = 100$ mm;
2. three different DAO sets of (0″, 0″, 0″), (0″, 0″, 0.″5), and (0″, 0″, 0.″9);
3. horizontal linear polarization;
4. two laser beam wavelengths of $\lambda = 532$ nm and $\lambda = 1064$ nm;
5. normal incidence of the laser beam on the CCR front face;
6. uncoated Suprasil 311 fused silica CCR (index of refraction $n = 1.456$–1.463); and
7. reflectivity $\rho; = 0.93$.

The results of the above six simulations are shown in Figures 7–12. For each simulation we plot

1. top panel, the FFDP;
2. middle panel, the laser return intensity distribution in OCS units versus VA; and
3. bottom panel, the laser return intensity distribution in OCS units at the most probable VA on the Moon (between 1.″0 and 1.″1, or equivalently between 4.84 and 5.33 μrad) versus the azimuthal angle of the pattern.

Note that the pixel size is 0.364×10^{-6} rad (0.″075) for Figures 7–9 at 532 nm and twice that for Figures 10–12 at 1064 nm.

The laser returns of Figures 7–12 are shown in OCS units, i.e., in Msqm (million square meters, Mm^2). These units derive

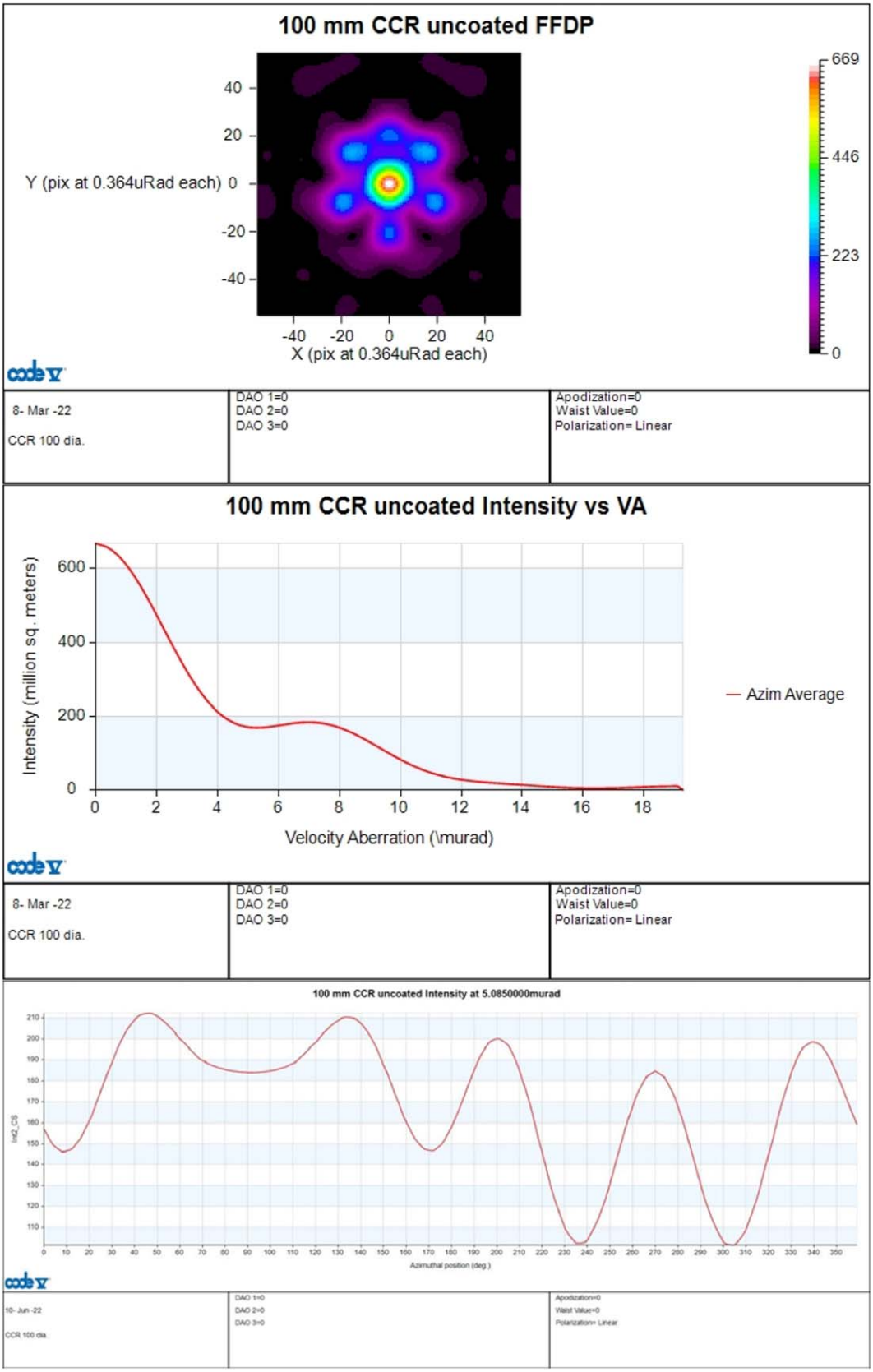

Figure 7. $\lambda = 532$ nm, linear polarization, and DAO = (0″, 0″, 0″). Top: FFDP; middle: OCS vs. VA; bottom: OCS at VA 1.″05 vs. azimuth angle.

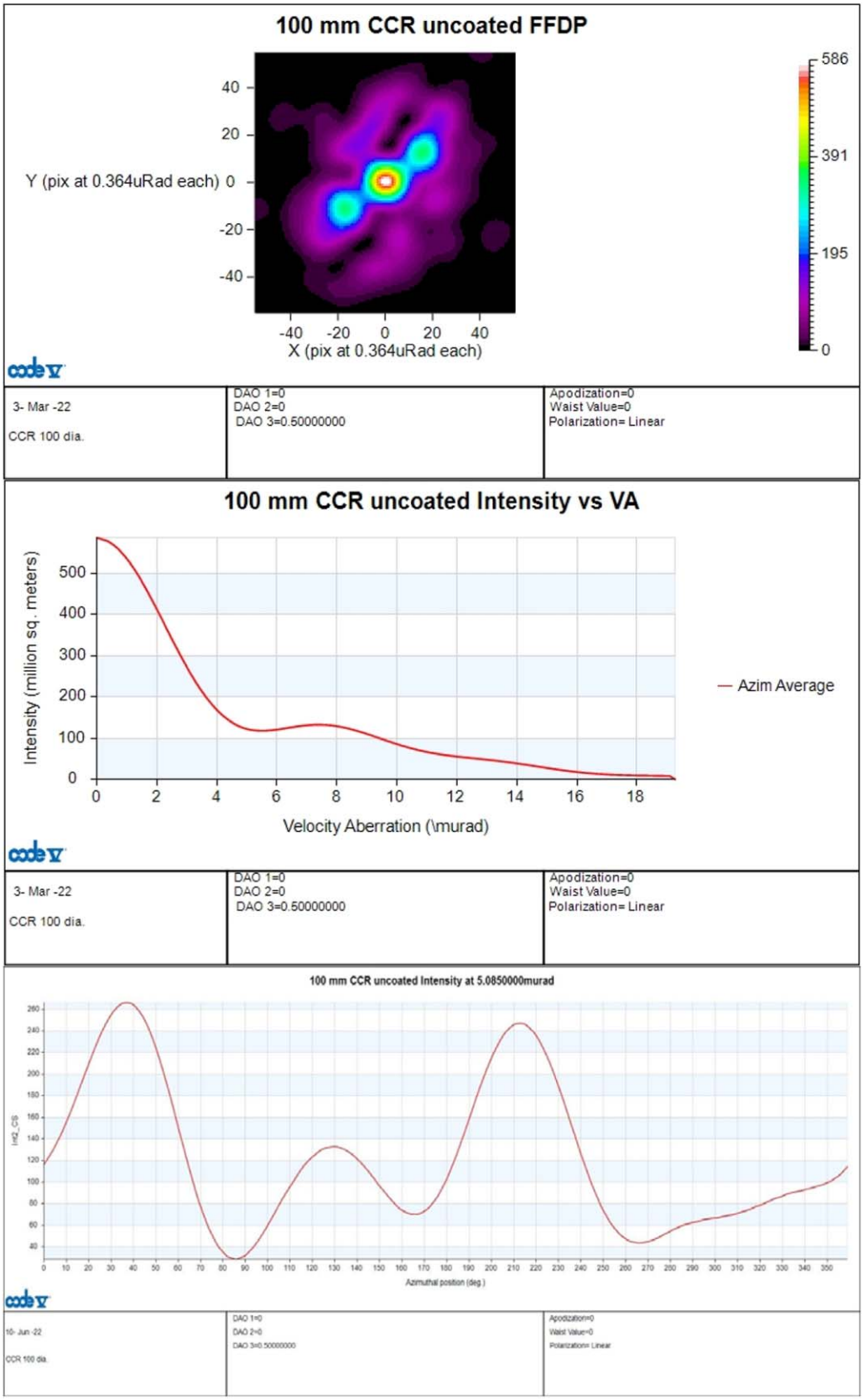

Figure 8. $\lambda = 532$ nm, linear polarization, and DAO $= (0'', 0'', 0\overset{''}{.}5)$. Top: FFDP; middle: OCS vs. VA; bottom: OCS at VA $1\overset{''}{.}05$ vs. azimuth angle.

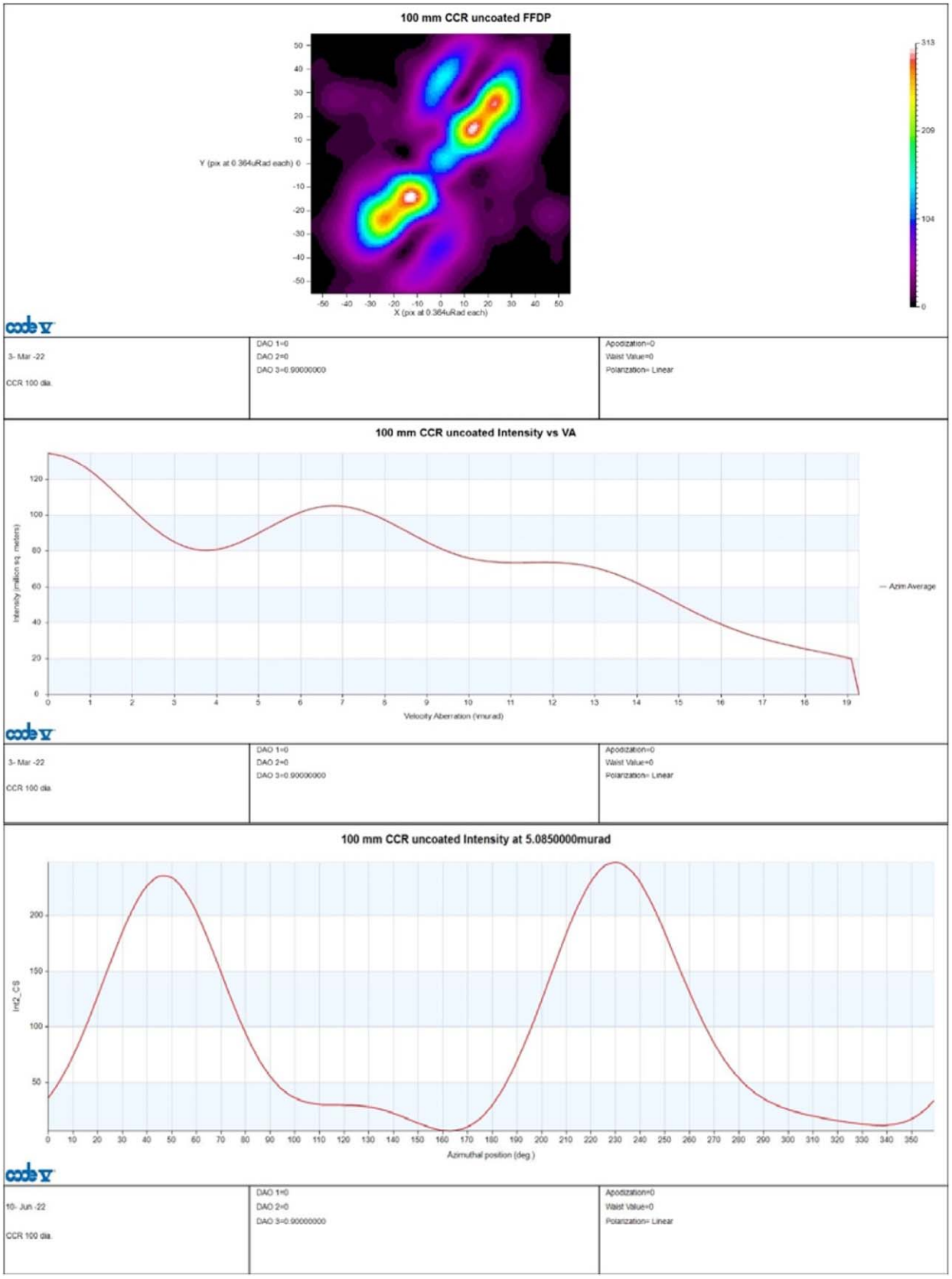

Figure 9. $\lambda = 532$ nm, linear polarization, and DAO $= (0'', 0'', 0\overset{''}{.}9)$. Top: FFDP; middle: OCS vs. VA; bottom: OCS at VA $1\overset{''}{.}05$ vs. azimuth angle.

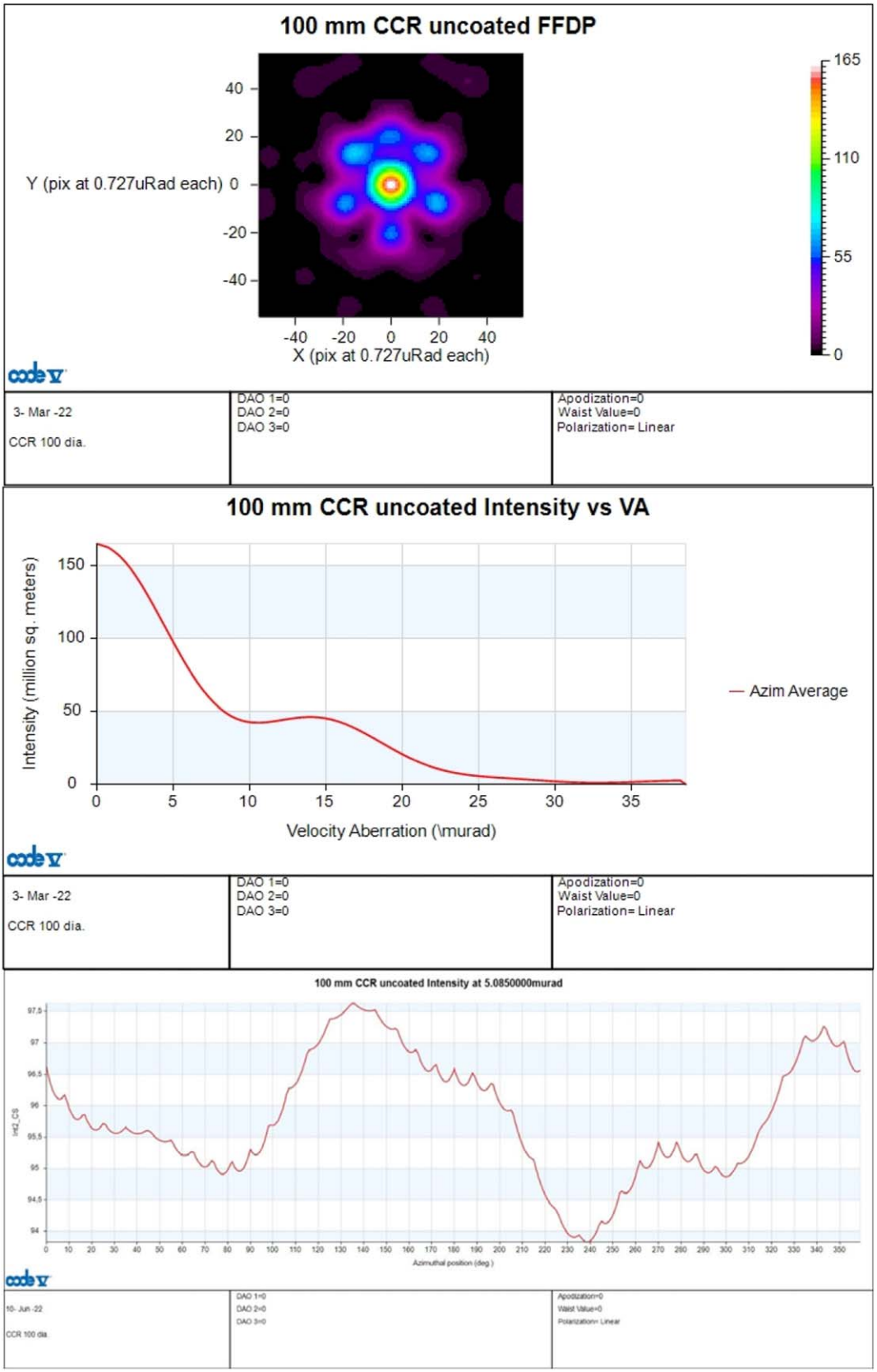

Figure 10. $\lambda = 1064$ nm, linear polarization, and DAO = (0″, 0″, 0″). Top: FFDP; middle: OCS vs. VA; bottom: OCS at VA 1.″05 vs. azimuth angle.

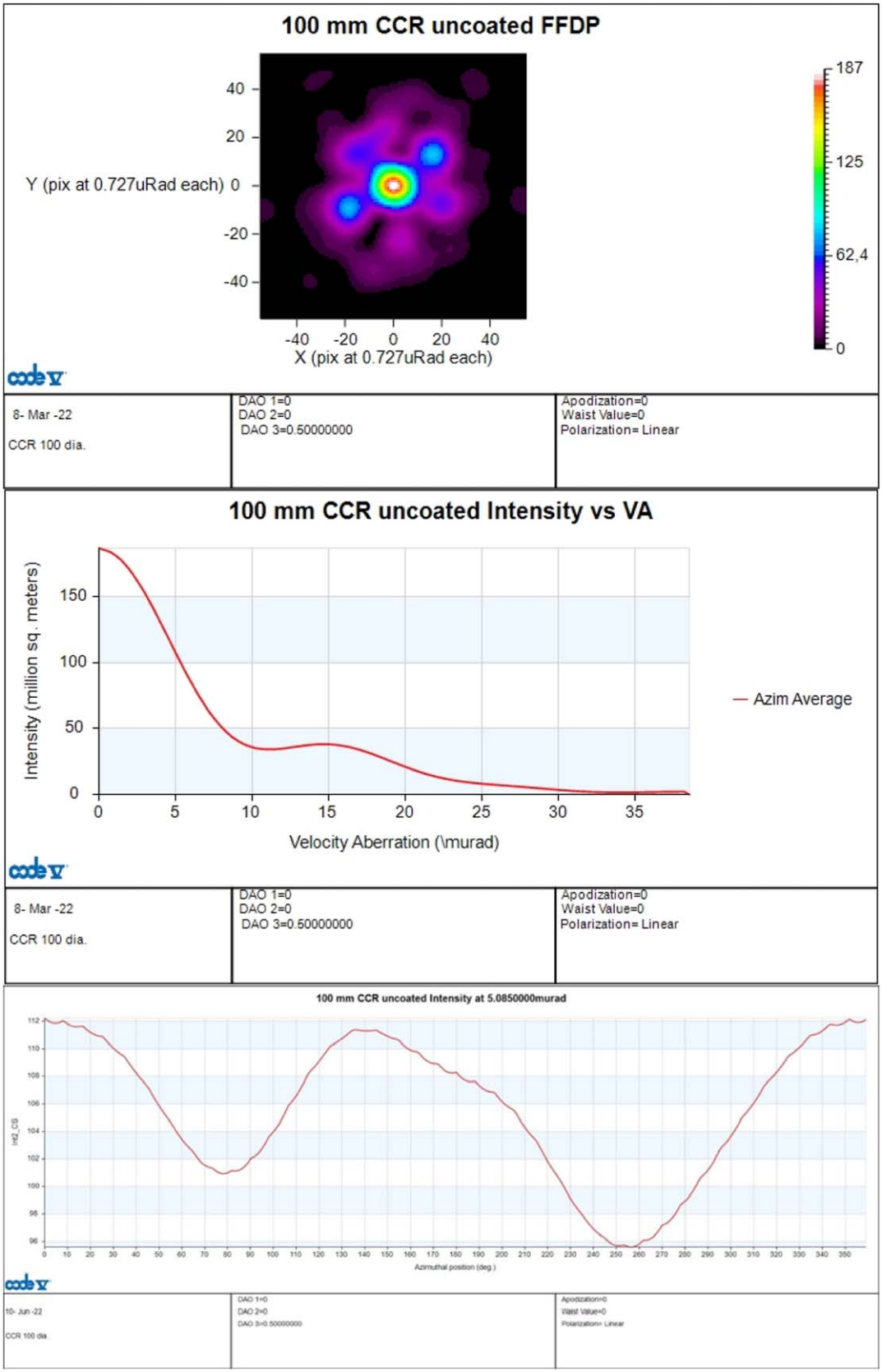

Figure 11. $\lambda = 1064$ nm, linear polarization, and DAO = ($0''$, $0''$, $0\overset{''}{.}5$). Top: FFDP; middle: OCS vs. VA; bottom: OCS at VA $1\overset{''}{.}05$ vs. azimuth angle.

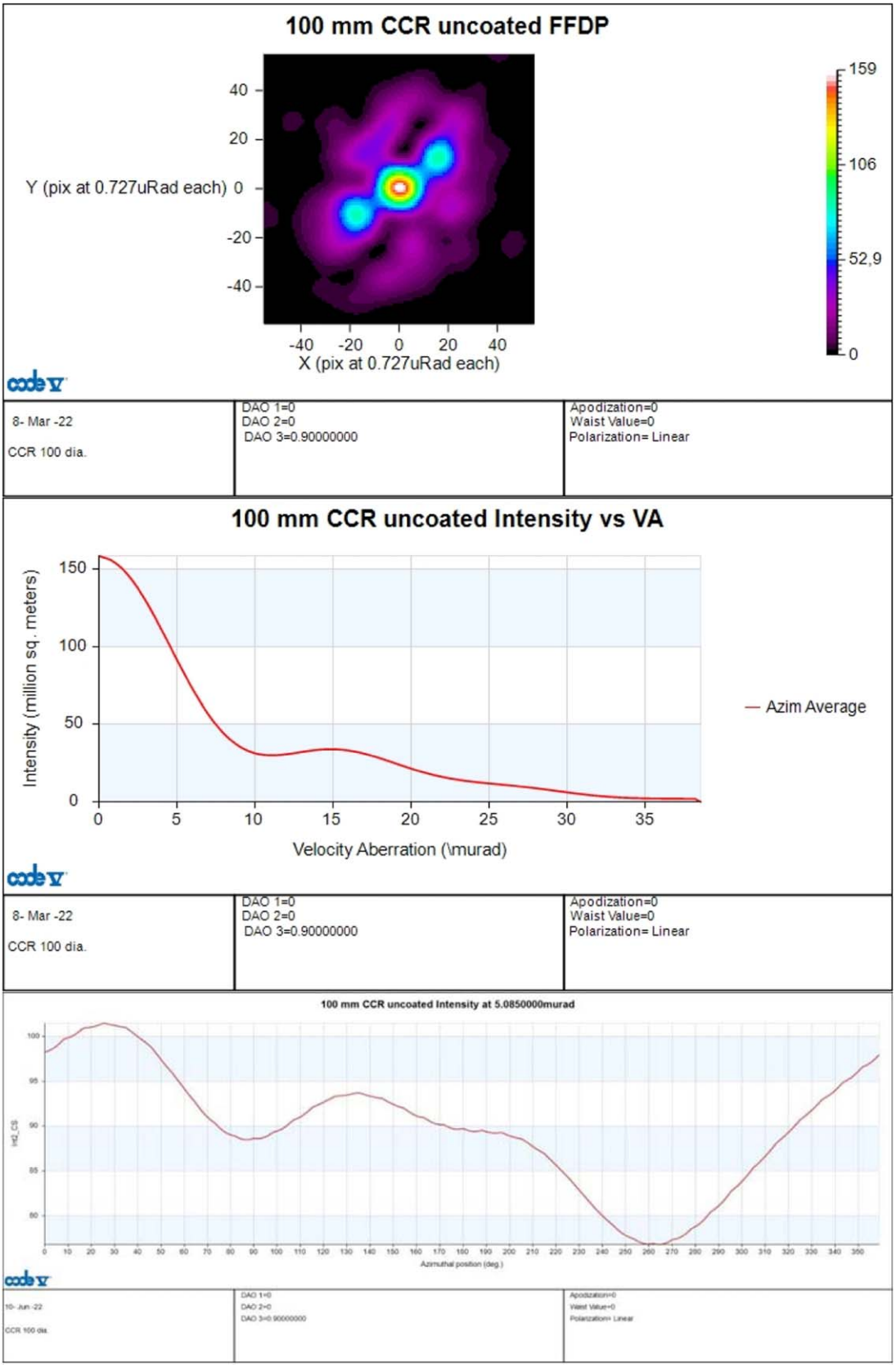

Figure 12. $\lambda = 1064$ nm, linear polarization, DAO = (0″, 0″, 0.″9). Top: FFDP; middle: OCS vs. VA; bottom: OCS at VA 1.″05 vs. azimuth angle.

from Degnan's equation describing the central peak of the laser return signal for a CCR with zero DAOs (Degnan 2012). In his formula

$$\mathrm{OCS} = p\left(\frac{\varrho\ \pi^3 D^4}{4\lambda^2}\right) = (168 - 670)\ \mathrm{Msqm} \qquad (1)$$

for normal incidence of the laser beam on the CCR front face. The lower limit on the peak of the OCS is attained for $\lambda = 1064$ nm (Figure 10), whereas the upper limit is for $\lambda = 532$ nm (Figure 7). The factor $p = 26.4\%$ describes the effect of the polarization and applies only in the case of uncoated CCRs (Murphy & Goodrow 2013). Nonzero DAOs reduce the value of the peak of the OCS in a nonlinear way, as we are going to see below.

This subsection presents linear polarization, and the next subsection presents circular polarization. There will be a discussion of results with tabulations after the next subsection.

6.2. MoonLIGHT/NGLR Simulations for Circular Polarization

In this section we consider right-handed circular polarization to be transmitted by a ranging station rather than linear polarization. Otherwise, the conditions are like those of the preceding subsection.

Figures 13–18 are analogous to Figures 7–12, respectively. Figures 13–15 are for $\lambda = 532$ nm with the DAO sequence of (0″, 0″, 0″), (0″, 0″, 0.″5), and (0″, 0″, 0.″9). Figures 16–18 are for $\lambda = 1064$ nm with the DAO sequence of (0″, 0″, 0″), (0″, 0″, 0.″5), and (0″, 0″, 0.″9).

6.3. Discussion of Simulations

The results for linear and circular polarization are summarized in Tables 5–7. Table 5 shows the spread OCS versus VA averaged over the full azimuth angle of the FFDP. For the Mare Crisium and Reiner Gamma sites, we are interested in VA values from 0.″8 to 1.″5 or from 3.88 to 7.27 μrad (Table 4). The larger OCS value corresponds to the smaller VA for five of the six cases, with DAO (0″, 0″, 0.″9) at 532 nm the exception. The noncentral peaks are ∼1.″5 from the center for 532 nm and twice that for IR.

Table 6 lists minimum and maximum OCS values at a typical VA of 1.″05 (5.09 μrad) versus azimuth angle. For existing LLR stations with a 20° elevation limit, the mean aberration is 1.″00 for APO, 1.″04 for MAT, 1.″06 for OCA/MeO, and 1.″10 for WZL. Consequently, 1.″05 is a good choice for the VA value in Table 6.

Generally, the DAO = (0″, 0″, 0″) cases are similar for both types of polarization. For $\lambda = 532$ nm and VA = 1.″05, there is approximately a factor of two variation of OCS with azimuth angle for both polarization types. For IR, those OCS variations are minor, 5%–10%. At $\lambda = 1064$ nm, the VAs of interest are closer to the central spot, so there is less variation with azimuth angle than for the shorter wavelength, as Table 6 shows.

For $\lambda = 532$ nm and DAO = (0″, 0″, 0.″5), the central spot is about 20% weaker for circular polarization, while the first ring is about 20% stronger. There is nearly a factor of five variation with azimuth angle for circular polarization, but the factor of eight variation is larger for linear polarization. The two maxima are about the same strength. For $\lambda = 1064$ nm, the central spot is about 10% weaker for circular polarization, while the first ring is about the same for both polarizations. Both polarization types vary with azimuth angle by only 10%–20%.

For $\lambda = 532$ nm and DAO = (0″, 0″, 0.″9), the central spot is about 15% weaker for circular polarization, while the first ring average is about 20% lower. The variation with azimuth angle is large for both polarizations. For $\lambda = 1064$ nm and DAO = (0″, 0″, 0.″9), the central spot is about 30% weaker for circular polarization, while the first ring is ∼20% stronger. The variation with azimuth angle is nearly a factor of two for circular polarization and ∼25% for linear polarization.

Nonzero DAOs shift OCS intensity from the central spot to the rings while splitting the FFDP into two parts along a line. This could benefit the return signal strength for VAs from 0.″8 to 1.″5, but it also increases variation with azimuth angle and requires proper orientation of the dihedral angle edge with respect to the lunar site's horizontal plane. Consequently, there is a trade-off. For both polarization types in Table 5, whereas at $\lambda = 1064$ nm the OCS span has low sensitivity to the choice of the DAOs, at $\lambda = 532$ nm the OCS span is more strongly affected by the DAOs. The trend, in this second case, is that the value of the OCS decreases for increasing values of the DAO. Moreover, looking at the bottom panels of Figures 7–9 and 13–15 and at Table 6, we conclude that at $\lambda = 532$ nm for larger DAOs the value of the OCS at the most probable VA for the Moon becomes less uniformly distributed with respect to the azimuth (clock) angle of the FFDPs. This effect is much less marked at $\lambda = 1064$ nm, as Figures 10–12 and 16–18 and also Table 6 show.

Table 2 gives the azimuth and elevation of the ME direction from the lander. But there is a third angle, the orientation of the rear dihedral angle edges of the CCRs with respect to the local horizontal. If the CCR edge with the nonzero DAO is oriented perpendicular to the mean VA direction, then the split FFDP is optimally oriented and the minimum value of each 360° span of values in Table 6 will not be reached. As can be seen from Figure 6, the largest spread of angles from the laser spot to the nearby corners occurs for the lowest-latitude LLR station, APO. That spread is ±24°. Consequently, Table 7 gives the minimum OCS value shifted ±24° from the peak value as a percentage compared to the peak value of 100%. With the DAO set (0″, 0″, 0″), the three dihedral angles are equivalent, but there is some sensitivity to orientation. With optimal DAO orientation, the IR return signal only varies by a few percent, but it varies by 20%–47% at $\lambda = 532$ nm. Together with percentage variations, it should be noted that the value of the OCS is generally higher by a factor of about two at 532 nm compared to 1064 nm (e.g., Table 6 shows that around 5 μrad for DAO = (0″, 0″, 0″), at 532 nm OCS ∼ 180–200 Mm^2, while at 1064 nm OCS ∼100 Mm^2).

Therefore, if the goal is to guarantee an optimal laser return at both $\lambda = 532$ nm and $\lambda = 1064$ nm and at all azimuth angles φ, it would be desirable to choose DAO set (0″, 0, 0″). Otsubo et al. (2010) reached a similar conclusion for $\lambda = 532$ nm.

6.4. Dihedral Angle Choices

The first NGLR CCR to Mare Crisium will have a DAO set of ∼(0″, 0″, 0.″5) and a split diffraction pattern.

The Satellite/lunar/GNSS laser ranging Characterization Facilities Laboratory at INFN-LNF has two MoonLIGHT CCRs:

1. One with DAOs of ∼(0″, 0″, 0.″5) is in house.

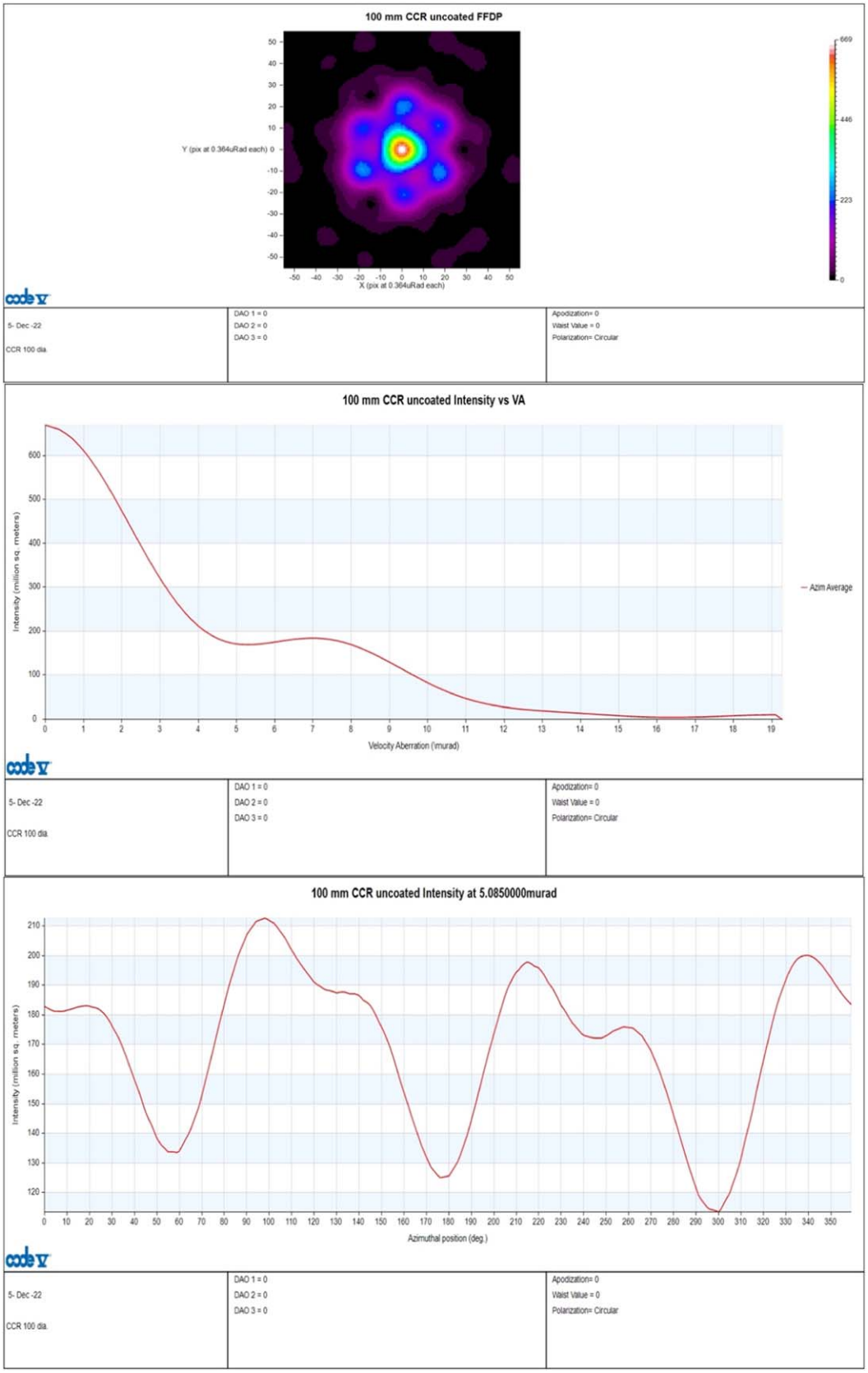

Figure 13. $\lambda = 532$ nm, circular polarization, and DAO = (0″, 0″, 0″). Top: FFDP; middle: OCS vs. VA; bottom: OCS at VA 1.″05 vs. azimuth angle.

2. A second one with DAOs of ∼(0″, 0″, 0″) is in house.

For the first launch of MoonLIGHT to Reiner Gamma, which one of the two CCRs to deploy is being evaluated.

6.5. Considerations

The size of the central spot in the FFDP is larger than the VA for the 3.8 cm Apollo CCRs, but for the 10 cm CCRs the first

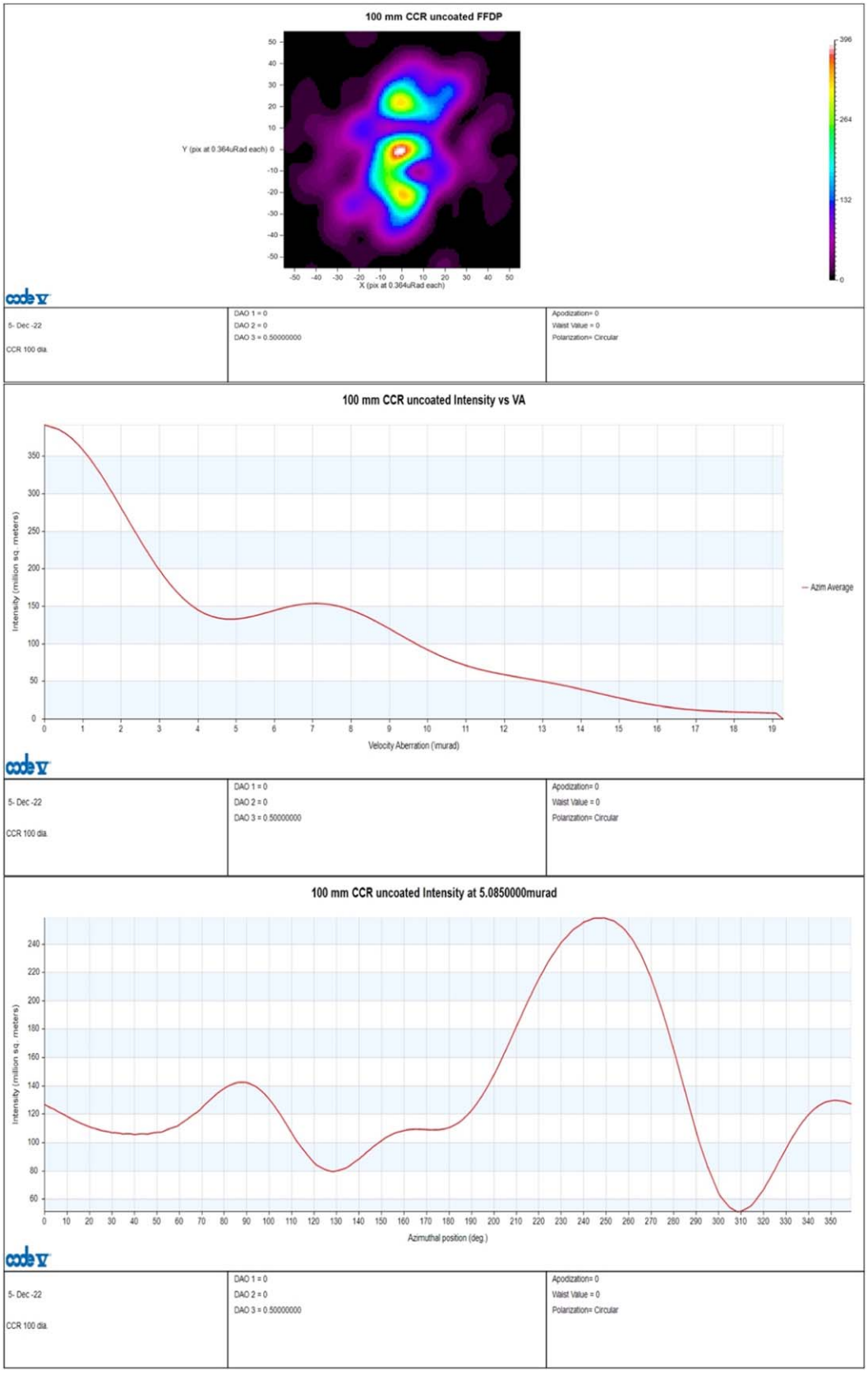

Figure 14. $\lambda = 532$ nm, circular polarization, and DAO = (0″, 0″, 0.″5). Top: FFDP; middle: OCS vs. VA; bottom: OCS at VA 1.″05 vs. azimuth angle.

minimum will have a ∼1.″1 radius for a frequency-doubled green Nd:YAG (532 nm) laser pulse, smaller than the maximum aberrations in Tables 3 and 4. Since the size of the FFDP is proportional to wavelength, the fundamental IR (1064 nm) wavelength would do better for VA for 10 cm CCRs but would have a lower peak intensity. The FFDP can be split into

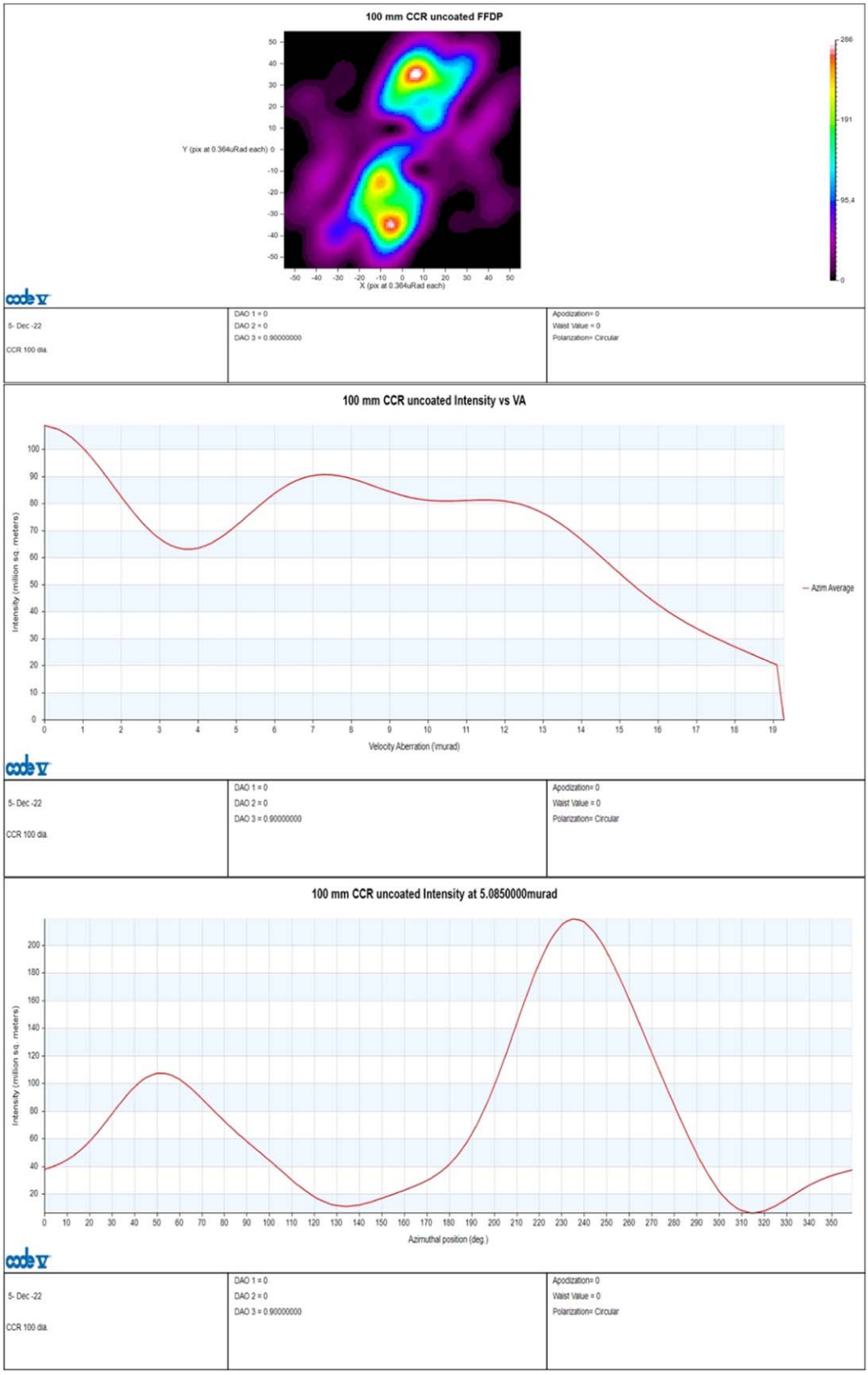

Figure 15. $\lambda = 532$ nm, circular polarization, and DAO = ($0''$, $0''$, $0\overset{''}{.}9$). Top: FFDP; middle: OCS vs. VA; bottom: OCS at VA $1\overset{''}{.}05$ vs. azimuth angle.

two lobes by slightly modifying one or more of the rear dihedral angles by a fraction of an arcsecond. If the CCR has an FFDP with two lobes (a diffraction pattern split into two lobes), then one of the two lobes should be aligned with the direction of the mean VA vector for optimum performance; otherwise, the return OCS would be lower (see below) than that of a CCR

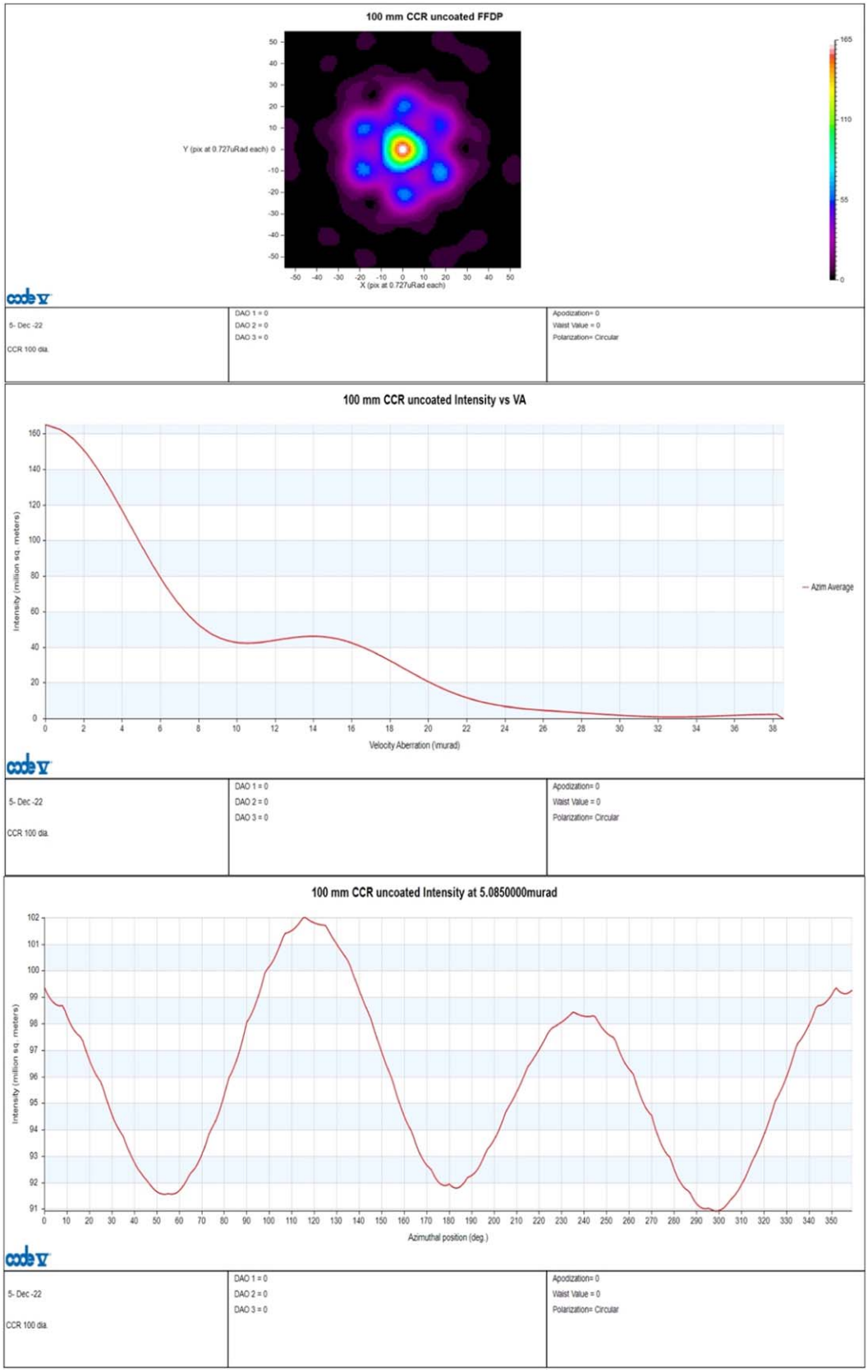

Figure 16. $\lambda = 1064$ nm, circular polarization, and DAO = (0″, 0″, 0″). Top: FFDP; middle: OCS vs. VA; bottom: OCS at VA 1.″05 vs. azimuth angle.

with null angle offsets (the second lobe is lost because it is in the opposite direction of the VA vector). Note that thermal degradations of the FFDP may shift the nominal OCS versus VA and azimuth angle.

In addition to the position of Earth in the reflected laser diffraction pattern (Figure 6) and the VA direction, there are several effects that cause the strength of the reflected laser beam to vary, including array tilt due to optical librations and

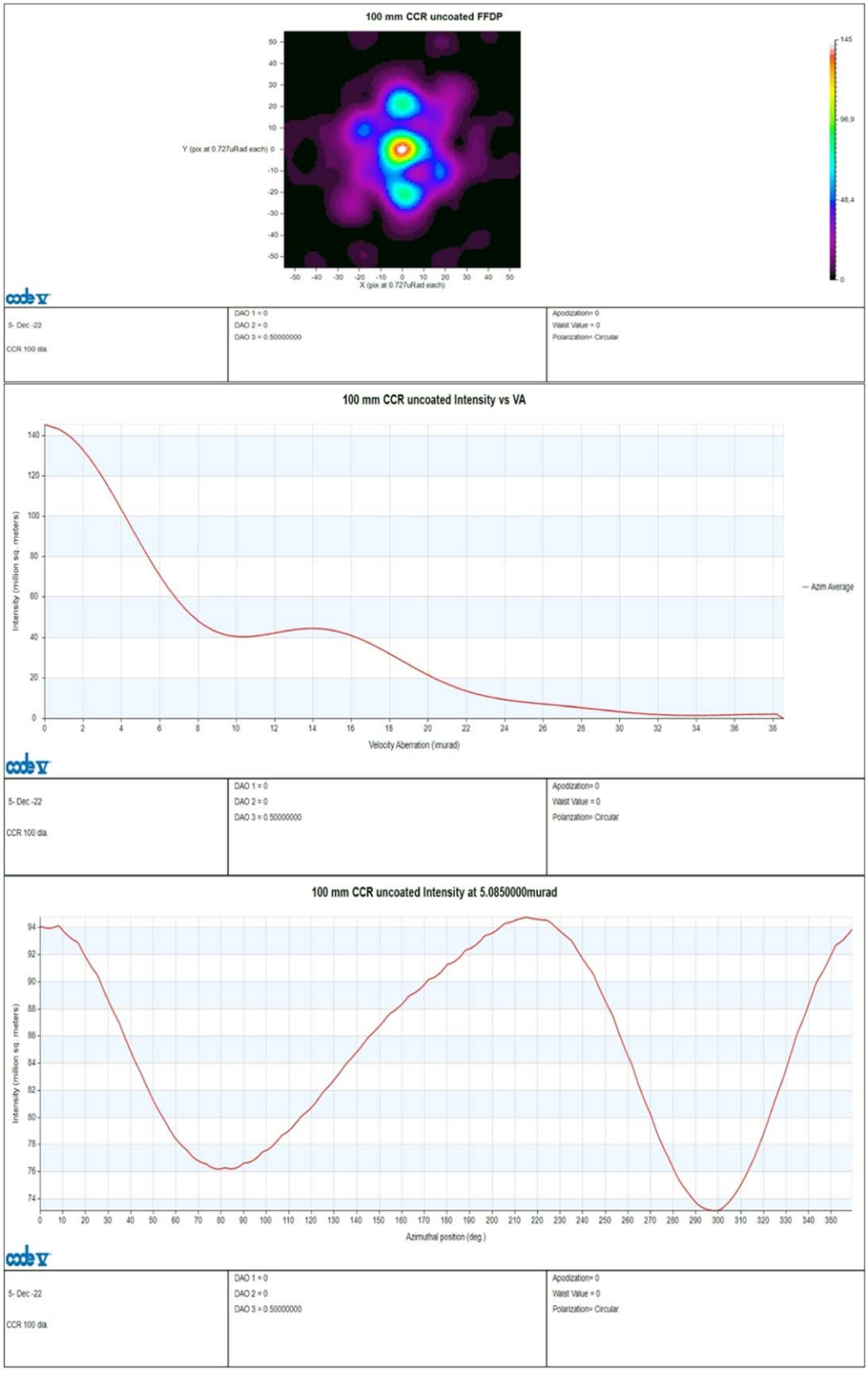

Figure 17. $\lambda = 1064$ nm, circular polarization, and DAO = $(0'', 0'', 0\overset{''}{.}5)$. Top: FFDP; middle: OCS vs. VA; bottom: OCS at VA $1\overset{''}{.}05$ vs. azimuth angle.

solar heating. We can minimize the tilt problems by orienting the normal to the CCR front face toward the ME direction. Properly oriented, the maximum tilt caused by optical librations is $11\overset{\circ}{.}5$ (Otsubo et al. 2010; Williams et al. 2022). That is less than the initial breakthrough angle of 17° for uncoated CCRs. Hui et al. (2020) find that polarized light illuminating a CCR

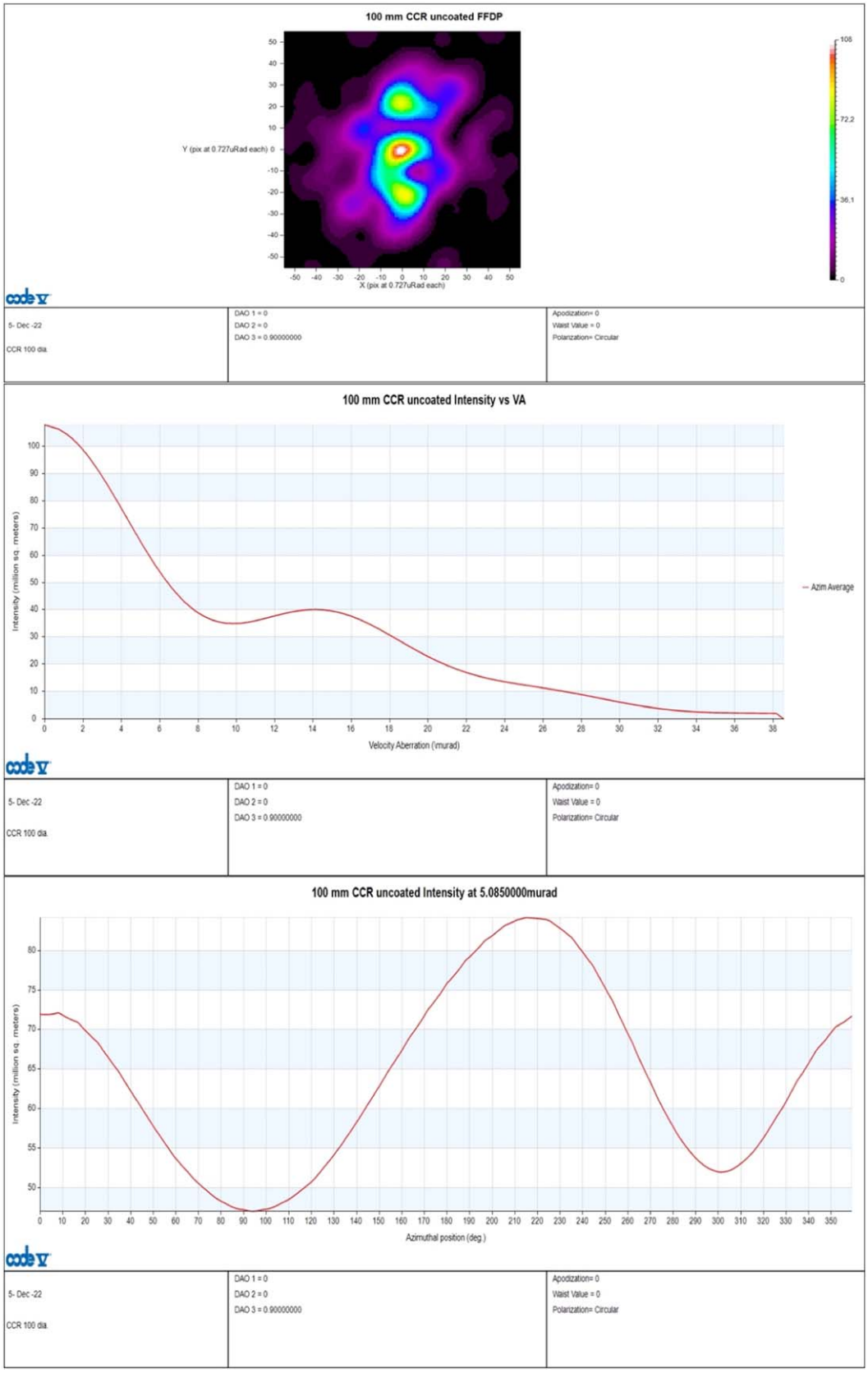

Figure 18. $\lambda = 1064$ nm, circular polarization, and DAO $= (0'', 0'', 0.''9)$. Top: FFDP; middle: OCS vs. VA; bottom: OCS at VA $1.''05$ vs. azimuth angle.

causes two strong noncentral spots in the FFDP. Tilting the array stretches the FFDP more in one direction. Circularly polarized light causes three strong noncentral spots in the FFDP. Arnold (2002) presents CCR transfer functions. Strategies to keep dust off of the CCR reduce temperature gradients from solar heating.

Table 5
Optical Cross Section Averaged over Azimuth Angle for VA = (3.88 to 7.27 μrad) or (0.″8 to 1.″5) for Two Wavelengths, Three DAO Sets, and Two Types of Polarization

Wavelength (nm)	Polarization	DAO = (0″, 0″, 0″) (Mm^2)	DAO = (0″, 0″, 0.″5) (Mm^2)	DAO = (0″, 0″, 0.″9) (Mm^2)
$\lambda = 532$	Linear	170–210	120–170	80–105
$\lambda = 1064$	Linear	60–120	55–120	50–110
$\lambda = 532$	Circular	170–210	135–155	65–90
$\lambda = 1064$	Circular	60–120	55–110	40–80

Table 6
Minimum and Maximum Values of Optical Cross Section vs. Azimuth Angle at VA = 5.085 μrad or 1.″05 for Two Wavelengths, Three DAO Sets, and Two Types of Polarization

Wavelength (nm)	Polarization	DAO = (0″, 0″, 0″) (Mm^2)	DAO = (0″, 0″, 0.″5) (Mm^2)	DAO = (0″, 0″, 0.″9) (Mm^2)
$\lambda = 532$	Linear	100–210	30–260	0–240
$\lambda = 1064$	Linear	93–98	96–112	76–101
$\lambda = 532$	Circular	115–210	50–260	10–220
$\lambda = 1064$	Circular	91–102	73–95	47–84

Table 7
Compared to a 100% Peak Value, the Minimum OCS Value in Percent Displaced ±24° in Azimuth Angle from the Maximum OCS Value

Wavelength (nm)	Polarization	DAO = (0″, 0″, 0″) (%)	DAO = (0″, 0″, 0.″5) (%)	DAO = (0″, 0″, 0.″9) (%)
$\lambda = 532$	Linear	80	53	64
$\lambda = 1064$	Linear	97	99	96
$\lambda = 532$	Circular	77	77	72
$\lambda = 1064$	Circular	97	97	94

Accounting for VA, Otsubo et al. (2010) recommend zero DAOs for 10 cm uncoated CCRs and three DAOs of 0.″25 for uncoated CCRs of 20 cm size or larger. The first 10 cm NGLR has a single 0.″5 DAO. A 0.″5 DAO causes the diffraction pattern to split by approximately ±1.″5. The 10 cm MoonLIGHT study (Sections 6.1 and 6.2) favors a zero DAO, but CCRs with both zero and 0.″5 DAOs exist. Which one to fly first is under consideration.

7. Pulse Spread

LLR data analysis fits range normal points, not the more numerous photon returns. A range normal point is constructed by combining the individual photon returns during a time span from a few minutes to a few tens of minutes. The lunar retroreflectors currently deployed on the lunar surface are arrays of smaller CCRs. Due to the lunar optical librations in orientation, the direction to the Earth center varies ±0.08 rad rms in two directions, up to ±0.14 rad in lunar longitude, and up to ±0.12 rad in latitude (Appendix in Williams et al. 2022). Including the angular size of Earth, the resulting temporal spread of the return laser photons in a normal point is equivalent to an rms range spread of 1–3 cm rms with extrema of ±3 cm (Lunokhods), ±6 cm (Apollos 11 and 14), and ±11 cm (Apollo 15) (see the 2022 Appendix).

The spread on reflection is in addition to the temporal length of the transmitted laser pulse and timing noise. Due to large improvements in laser technology and commercially available products, the effect of optical librations increases the size of the precision and contributes to the uncertainties in the analysis of the LLR data. If a retroreflector consists of a single large CCR, then the precision of the measurement of the time of flight depends on the precision of the timing of the transmitted and returned pulse and the length of the transmitted pulse. The range uncertainty then depends on the accuracy and precision of the timing electronics and the pulse length. On the Moon we must consider the temperature expansion and contraction of the retroreflector support structure, which may be much less than a millimeter if anchored in the regolith but can be several millimeters if sitting on top of a lander.

8. Polarization

There are six different ways that a photon can bounce three times in a CCR to retroreflect, and each generates a different orientation of reflected polarization. Consequently, when linear polarization is transmitted by the telescope at the LLR station, the reflection cross section of the NGLRs is dependent on the direction of polarization with respect to the CCR's dihedral angle edges. At $\lambda = 532$ nm with no DAO, Table 6 shows the cross section varying by a factor of two, but Table 7 shows that this is reduced to about 20% for optimal orientation of the edges. Murphy & Goodrow (2013, Figure 6) show that linear polarization introduces an asymmetry in the FFDP that, when the direction of polarization is rotated with respect to an edge, the asymmetry rotates by twice that and in the opposite direction. The asymmetry causes the bottom panel of Figure 7 to have five peaks of different heights rather than six of equal

Table 8
Extreme Rotation of Laser Horizontal to Lunar Equator for Stations' Negative and Positive Hour Angles (HAs) at the Maximum North and South Declinations δ for a 20° Elevation Limit

Station	Lat (deg)	Min S δ Neg HA (deg)	Min S δ Pos HA (deg)	Max N δ Neg HA (deg)	Max N δ Pos HA (deg)
APO	32.6	–89	89	–89	89
MAT	40.5	–86	86	–89	89
OCA/MeO	43.6	–30	30	–89	89
WZL	49.0	–30	30	–89	89

height. An optimum magnitude of the return signal would result if the LLR station maintains the polarization of the transmitted pulse to be parallel to the aberration direction. This is true for all three DAOs. At $\lambda = 1064$ nm, the aberrations of interest are closer to the central spot and the variations are much reduced. Table 7 shows that circular polarization has less sensitivity to nonzero DAOs.

There are practical considerations at the stations. The laser is too big and heavy to mount on smaller telescopes. Consequently, the unmoving laser is located at the coudé focus for the MAT, OCA/MeO, and WZL stations. The APO laser is located on the 3.5 m telescope at a Nasmyth port. Of the operational stations, OCA/MeO, WZL, and APO send a linear polarized laser beam into the telescope. APO uses S polarization. MAT sends circular polarization. The coudé sequence of mirrors modifies the polarization.

During the span of time of a ranging session at a station, the hour angle (HA) of the Moon deceases by $14\overset{\circ}{.}5\ \mathrm{hr}^{-1}$. As seen at the telescope's coudé focus, the apparent orientation of the Moon rotates. Consequently, for a fixed linear polarization direction at the coudé focus, the direction of polarization projected on the Moon rotates with respect to the lunar equator during a ranging session. For horizontal polarization at the laser output into the telescope, the extremes of the polarization direction with respect to the lunar equator are given in Table 8. A 20° elevation limit was used for each station. As can be seen, there are large variations in the polarization direction for all stations. For completeness, we include MAT in the table even though it does not send linear polarization into the telescope. The Moon can get as far south (S) as decl. $\delta = -28\overset{\circ}{.}6$ and as far north (N) as decl. $\delta = +28\overset{\circ}{.}6$; the elevation can dip below the 20° limit for stations north of $41\overset{\circ}{.}4$ (90°–$28\overset{\circ}{.}6$–$20\overset{\circ}{.}0$), hence the smaller spread of southern HAs for OCA/MeO and WZL. To get the angles with respect to the local horizontal at each reflector site, we must apply the rotations of the ME Azimuth column of Table 2 differenced from 180°: 180°–100° = 80° clockwise for Mare Crisium and 180° − 94° = 86° counterclockwise for Reiner Gamma.

For retroreflected laser light exiting a corner cube at the front face, there are six segments, each 60° wide, with its own polarization. The span of HAs in Table 8 is 60° (at minimum decl. δ south $-28\overset{\circ}{.}6$) to 178° (at maximum decl. δ north $+28\overset{\circ}{.}6$). Consequently, the reflected light at large distances will cycle through brighter and fainter reflections during a long ranging session. Table 7 shows that for a VA of $1\overset{''}{.}05$ and no DAO this cycling is about 20% at 532 nm, but only a few percent at 1064 nm. For a DAO of $0\overset{''}{.}5$ at 532 nm, the variation can reach 47%.

9. Range Equipment and Model

The new retroreflectors do not spread the pulse during reflection. Consequently, there is motivation to reduce the uncertainty due to the ranging equipment at the stations.

To analyze the improved range data, upgraded data analysis models are also needed. The current JPL model is described by Park et al. (2021) and Williams & Boggs (2020). For example, we do not currently model the effect of horizontal pressure gradients on the atmospheric delay at a station. There are a variety of loading effects (Singh et al. 2021), only some of which we model. In addition, the effect of the lunar inner core on the physical librations remains to be determined. Different models are discussed by Pavlov et al. (2016) and Viswanathan (2017).

10. Conclusions

Table 1 gives information on existing lunar retroreflectors and the proposed NGLR and MoonLIGHT retroreflectors. Section 2 gives a brief history of range uncertainty. Section 4 and Table 2 give the schedule and landing locations of the first two 10 cm CCRs. VA is discussed in Section 5, and its distribution is given in Table 3. The extremes of VA are presented in Table 4, and the effect of station latitude is shown in Figure 6.

The FFDP of the 10 cm CCRs is the subject of Section 6. Figures 7–18 illustrate the calculated FFDP for three DAOs and two wavelengths for linear and circular polarization. The return strength versus VA and azimuthal angle are also illustrated. It is concluded that zero DAO is optimum for green and IR laser beams. Section 7 discusses the NGLR and MoonLIGHT CCRs.

For optimum performance, linear polarization should be aligned with the VA direction (Section 8), but practical considerations may make this difficult. To take advantage of improved range precision, Section 9 advocates improved station equipment and data analysis models. The 10 cm CCRs should enable improved lunar science, terrestrial geodesy, and gravitational physics results from LLR.

We thank the LLR stations at McDonald Observatory, Texas; Observatoire de la Côte d'Azur, France; Haleakala Observatory, Hawaii; Apache Point Observatory, New Mexico; Matera, Italy; and Wettzell, Germany, which provided the data sets that make LLR analyses possible. LLR data are available from the Crustal Dynamics and International Laser Ranging Service archive at https://cddis.nasa.gov/Data_and_Derived_Products/SLR/Lunar_laser_ranging_data.html. We thank Nicolas Colmenares of Goddard Space Flight Center for information on the Apache Point laser and telescope. The effort by INFN-LNF authors is supported by ESA under contract No. 4000129000/19/NL/TFD (and a NASA-ESA MoU for CP-11) and by ASI under agreement No. 2019-15-HH.0. D.G.C. acknowledges the support of NASA under contract No. 80MSFC20C0012 (LSITP). A portion of the research described in this paper was carried out at the Jet Propulsion Laboratory, California Institute of Technology, under a contract with the National Aeronautics and Space Administration (80NM0018D0004). Government sponsorship acknowledged.

ORCID iDs

James G. Williams https://orcid.org/0000-0002-8441-5937
Luca Porcelli https://orcid.org/0000-0002-2153-4242

Dell'Agnello https://orcid.org/0000-0002-0691-8213
Marco Muccino https://orcid.org/0000-0002-2234-9225
Douglas G. Currie https://orcid.org/0000-0002-6177-9826
Dennis Wellnitz https://orcid.org/0000-0002-6607-8949
Chensheng Wu https://orcid.org/0000-0002-8414-4487
Dale H. Boggs https://orcid.org/0000-0002-1568-3428

References

Arnold, D. 2002, Retroreflector Array Transfer Functions, Proc. 13th Int. Workshop on Laser Ranging
Bagheri, A., Efroimsky, M., Castillo-Rogez, J., et al. 2022, AdGeo, 63, 231
Chapront-Touzé, M., & Chapront, J. 1988, A&A, 190, 342
Ciocci, E., Martini, M., Contessa, S., et al. 2017, AdSpR, 60, 1300
Crawford, I. A., Anand, M., Cockell, C. S., et al. 2012, P&SS, 74, 3
Currie, D. G., Dell'Agnello, S., Delle Monache, G. O., Behr, B., & Williams, J. G. 2013, NuPhB, 243, 218
Degnan, J. J. 2012, in A Tutorial on Retroreflectors and Arrays for SLR, ILRS Workshop, https://ilrs.gsfc.nasa.gov/docs/2012/degnan_retrotutorialppt_121105
ESA 2019, ESA Strategy for Science at the Moon, https://exploration.esa.int/s/WmMyaoW
Garattini, M., Dell'Agnello, S., Currie, D., et al. 2013, AcPol, 53, 821
Goodrow, S. D., & Murphy, T. W., Jr. 2012, ApOpt, 51, 8793
Haviland, H. F., Weber, R. C., Neal, C. R., et al. 2022, PSJ, 3, 21
Hui, Z., Song, L., Wenhao, Z., & Yuwei, C. 2020, ApOpt, 59, 2621
Kawamura, T., Grott, M., Garcia, R., et al. 2022, ExA, 54, 617
Martini, M., Dell'Agnello, S., Currie, D., et al. 2012, P&SS, 74, 276
Merkowitz, S. M., Dabney, P. W., Livas, J. C., et al. 2007, IJMPD, 16, 2151
Mohr, P. J., Newell, D. B., & Taylor, B. N. 2016, RvMP, 88, 035009
Müller, J., Murphy, T. W., Jr., Schreiber, U., et al. 2019, JGeod, 93, 2195
Murphy, T. W., Jr., Adelberger, E. G., Battat, J. B. R., et al. 2010, Icar, 208, 31
Murphy, T. W., Jr., Adelberger, E. G., Battat, J. B. R., et al. 2011, Icar, 211, 1103
Murphy, T. W., Jr., & Goodrow, S. D. 2013, ApOpt, 52, 117
Murphy, T. W., Jr., McMillan, R. J., Johnson, N. H., & Goodrow, S. D. 2014, Icar, 231, 183
NASA 2019, Science Strategy at the Moon, https://sservi.nasa.gov
Otsubo, T., Kunimori, H., Noda, H., & Hanada, H. 2010, AdSpR, 45, 733
Otsubo, T., Kunimori, H., Noda, H., et al. 2011, EP&S, 63, e13
Park, R. S., Folkner, W. M., Williams, J. G., & Boggs, D. H. 2021, AJ, 161, 15
Pavlov, D. A., Williams, J. G., & Suvorkin, V. V. 2016, CeMDA, 126, 61
Porcelli, L., Currie, D. G., Muccino, M., et al. 2021, Next Generation Lunar Laser Retroreflectors for Fundamental Physics and Lunar Science, The Committee on the Biological and Physical Sciences Research in Space 2023–2032, The National Academies of Sciences
Preston, A., & Merkowitz, S. 2013, ApOpt, 52, 8676
Preston, A., & Merkowitz, S. 2014, OptEn, 53, 065107
Singh, V. V., Biskupek, L., Müller, J., & Mingyue, Z. 2021, AdSpR, 67, 3925
Turyshev, S. G., Shao, M., & Hahn, I. 2021, Fundamental Physics and Lunar Science Investigations with Advanced Lunar Laser Ranging, The Decadal Survey on Biological and Physical Sciences (BPS) Research in Space 2023-2032, The National Academy of Sciences
Turyshev, S. G., Williams, J. G., Folkner, W. M., et al. 2013, ExA, 36, 105
Viswanathan, V. 2017, PhD thesis, Observatoire de Paris, https://hal.science/tel-01792665/
Williams, J. G., & Boggs, D. H. 2020, The JPL Lunar Laser Range Model 2020, JPL IOM 335N-20-01, https://ssd.jpl.nasa.gov/ftp/eph/planets/ioms/
Williams, J. G., Boggs, D. H., & Currie, D. G. 2022, PSJ, 3, 136
Zacny, K., Currie, D., Paulsen, G., Szwarc, T., & Chu, P. 2012, P&SS, 71, 131